Modeling of Water Transport in Highly Saturated Concrete with Wet Surface During Freeze/thaw

Fuyuan Gong[1] and Stefan Jacobsen[2]*

[1]Fellow of Strategic Innovation Program, Department of Civil Engineering, The University of Tokyo, Hongo 7-3-1, Bunkyo, Tokyo 113, JAPAN
[2]Professor, Department of Structural Engineering, Norwegian University of Science and Technology, Trondheim, NORWAY

ABSTRACT

Wet frost exposure is a usual environmental condition for cement-based materials (CBM) during winter and the most common way of frost testing in the lab. In this study, the temperature gradient, pressure gradient, and the liquid flow under wet frost exposure are modeled for highly saturated CBM with different amount of entrained air. It is found that the water uptake happens at the melting stage, and for non-air-entrained CBM, the hydraulic pumping effect is dominant and will suck the water from wet surface. While for air-entrained CBM, the cryosuction pressure is the main driving force of the inward flow. The results are compared with experimental data from rapid freeze/thaw testing of various types of concrete in water, showing a satisfactory agreement. Sensitivity analysis also indicates that the hydraulic induced flow depends on the amount of entrained air, while the cryosuction induced flow mainly relies on the permeability and temperature gradient.

Keywords: water transport, cement-based materials, wet frost exposure, highly saturated.

1. Introduction

The public infrastructures play an important role in the economic development but need a huge amount of money, so it will also become a heavy burden if the service lives of those infrastructures become too short. The concrete structures and materials themselves will gradually deteriorate due to the environmental impact, such as frost action, chloride ion, carbonation and so on. For all these deterioration factors the moisture condition plays a key role because it directly affects almost all the physical and mechanical process inside the material. The wet frost exposure is a typical situation in cold and wet regions, in which free water can be present at the surface and a temperature gradient is generated in the material due to the ambient temperature change. Under such a case the liquid transport would be largely accelerated. The accelerated absorption due to freezing and thawing is clearly seen during freeze/thaw testing as a new absorption starting beyond the capillary saturation level obtained on the specimens at ordinary capillary suction before the freeze/thaw exposure starts, see for example [1-9].

The driving force of this accelerated transport of external liquid going into the material was discussed in previous studies and it was owed to the negative pressure created during phase transition of pore water to ice under the highly saturated condition [10], also known as cryosuction. Due to the surface tension of crystal-liquid interface, the pressure of the unfrozen pore water should decrease in order to achieve a thermodynamic equilibrium, and the value of this pressure is closely related to the local temperature [11]. According to Darcy's law, this would result in the liquid water flow in addition to the pumping effect of hydraulic pressure caused by volume expansion of ice. This hydraulic pressure may also cause damage to CBM, and the permeability would increase if frost damage in the form of internal cracking occurs [12], and as a result, the liquid flow can be much accelerated. Another effect of freezing on the permeability is that, once the bigger pores are occupied by ice, the liquid permeability would decrease drastically, which has been discussed in Coussy [13], but this permeability change is temporary only when ice exists inside the body and would not affect permeability ahead of a propagating ice front.

In-depth transport studies of concrete exposed to freeze/thaw are rare, both because the modeling becomes complicated and there are few measurements available to verify models with. Models of flow in concrete during exposure to frost and liquid at the surface are complex because of the variation of both temperature and access of liquid at the surface depending on presence of ice or liquid at the surface. Thus, the boundary conditions become complicated for many reasons, as do the transfer equations.

In field or on real structures we are not aware of any measurements of flow in hardened concrete during frost exposure under varying conditions of temperature variations and liquid at the concrete surface. In the laboratory testing of freeze/thaw resistance or deicer salt scaling resistance one usually only measures the damage, either as internal cracking or as surface scaling. In a few cases both scaling and cracking are measured simultaneously. However, there are even fewer measurements on the flow of liquid during freeze/thaw. In this paper we include some reviewed data on this kind of transport in concrete during freeze/thaw exposure and used them for comparison with our numerical modeling. Hopefully this will improve the understanding of how wet concrete freeze/thaw tests, i.e where the specimen surface is always wet or covered with ice, work.

Therefore, in this study, we propose a physical and numerical model, which can include most of the main factors mentioned above. This is done by simulating the temperature, ice content and permeability change during one freeze/thaw cycle sequentially, and then applying this information in the stress model to calculate the driving forces. After that, the water flow is simulated considering different environmental conditions and boundary conditions, and further compared with previous experimental data. Finally, the sensitivities of several influential parameters are discussed as well.

This work mainly deals with transport calculations into materials that are initially highly saturated, so that the normal capillary absorption can be excluded. In addition, the material can be damaged by frost action but within limited levels, so that the continuum mechanics can still be used to describe the physical and mechanical process.

2. Local thermodynamic equilibrium

The most typical wet frost exposure condition is considered and modelled in this study, where one surface is in contact with the free water directly, and with the controlled temperature, see Fig. 1. The thickness here is assumed to be 50mm, and the temperature range is T_{max}=4^{o}C, T_{min}=-18^{o}C, resembling the exposure during the ASTM C666 Procedure A test. In such a case, once the temperature falls below 0^{o}C, the free water on the wet surface would freeze and liquid water would no longer flow into the material. But during the melting process, the wet surface would melt while the temperature inside partly still stays below 0^{o}C. Such wet frost exposure is quite common in real life, like on bridge decks and highways with free water on the top, which will stay as liquid during daytime or when exposed to direct sunlight but freeze at night or when shaded. Accelerated lab tests such as ASTM 666C Procedure A, SS 137244 and CDF/CIF are equivalent to this boundary condition.

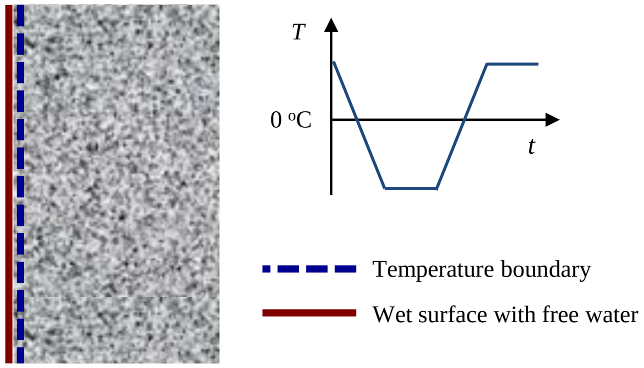

Fig. 1 The basic model and boundary conditions

More precisely, the heat transfer and moisture movement are coupled during this process [14]. For example, the thermal conductivity of the material should change slightly during phase change of moisture, additional heat flow would be generated when ice forms, and the liquid flow might also transfer heat. However, practically speaking, the influence by the moisture is very limited so that we can still approximately regard them as independent. In addition, for the heat liberated or consumed by ice on freezing or melting, since only about a quarter of the water in a saturated hardened CBM can freeze at normal freezing temperature [15], the amount of heat released by ice formation will have a negligible impact on the global temperature field in the solid matrix (see Appendix A), so the coupling can be ignored.

In sum, the temperature field can be a good approximation when imposed independently through the boundary conditions (such as natural cooling at the exposed surface). Using this known temperature distribution, other target variables can also be calculated independently.

2.1 Temperature, ice formation and permeability

2.1.1 Temperature

The temperature is controlled on the wet surface (x=0), with the temperature history shown in Fig. 1. The opposite surface (x=L) could be either constant temperature (first-type) or heat-insulated (second-type) boundary. The temperature at different depths and times $T(x,t)$ could be solved by the one-dimensional heat conduction equation for convenience:

For the constant-temperature boundary (first-type boundary):

$$\begin{cases} \dfrac{\partial T}{\partial t} = a \cdot \dfrac{\partial^2 T}{\partial x^2} \\ T(0,t) = f(t) \\ T(L,t) = T_{\max} \end{cases} \tag{1}$$

For heat-insulated boundary (second-type boundary):

$$\begin{cases} \dfrac{\partial T}{\partial t} = a \cdot \dfrac{\partial^2 T}{\partial x^2} \\ T(0,t) = f(t) \\ \left.\dfrac{\partial T}{\partial x}\right|_{x=L} = 0 \end{cases} \tag{2}$$

where $a=\lambda/(C_p \cdot \rho)$, and for concrete, the thermal conductivity $\lambda \approx 1.0$J/(s·m·K), heat capacity C_p=880J/(kg·K), density $\rho \approx 2400$kg/m^3, so $a=4.7\times10^{-7}$m^2/s or a=0.47mm^2/s.

2.1.2 Ice formation

For porous materials, the freezing point of liquid water depends on the curvature of crystal/liquid interface, which is [11]:

$$\kappa_{CL}\gamma_{CL} = \Delta S_{fv}(T_0 - T) \tag{3}$$

where κ_{CL} is the curvature of the crystal/liquid interface, γ_{CL} is the specific energy of the crystal/liquid interface (0.04N/m or J/m^2 for water-ice). $\Delta S_{fv}\approx$1.2J/(cm^3·K) is the molar entropy of fusion. T_0 is the freezing point of free water, here the pure water is assumed for convenience so that T_0=0°C. The curvature κ_{CL} can be also written as:

$$\kappa_{CL} = \frac{2\cos\theta_{CL}}{r-\delta} \tag{4}$$

where θ_{CL} is the contact angle of the crystal/liquid interface, which can be assumed as 0. r is the radius of the pore entry, and δ is the thickness of the liquid film between ice crystal and the pore wall (≈0.9nm). Given a certain temperature T (T<0), it is assumed here that all the pores that are bigger than r would freeze, while the rest would stay unfrozen. Therefore, the ice content (the volume fraction of pore space filled with ice) can be drawn as a function of temperature based on the pore size distribution. The pore size distribution varies with a number of parameters such as mix proportions, type of binder, curing conditions and ageing/deterioration mechanisms, which need to be measured for each particular experiment or empirically estimated. But those measurements or estimations are indirect and usually it is difficult to reflect the big hysteresis between the freezing and melting curves (Fig. 4). So here we think the freezing curve and melting curve for saturated paste can be approximated by:

$$S_{C_f} = -5\times10^{-6}T^3 - 6\times10^{-4}T^2 - 0.0262T \quad (-40^\circ\mathrm{C} \le T \le 0^\circ\mathrm{C}) \tag{5}$$

$$S_{C_m} = \frac{0.449T}{T-2.525} \quad (-40^\circ\mathrm{C} \le T \le 0^\circ\mathrm{C}) \tag{6}$$

The freezing curve and melting curve are not the same, because the freezing point is usually controlled by the size of pore entry while the melting point is by that of pore body [16], and the pore shape factor λ_p can be defined as:

$$\lambda_p = \frac{T_M - T_0}{T_F - T_0} \tag{7}$$

For the same amount of ice content in a given pore, T_M (melting) is always higher than T_F (freezing). Sun's experimental data show that λ_p is usually between 0.1 and 0.5 for cement-based materials [16].

$$\lambda_p = -0.0095T_F + 0.1251 \quad (-40^\circ\mathrm{C} \le T_F \le 0^\circ\mathrm{C}) \tag{8}$$

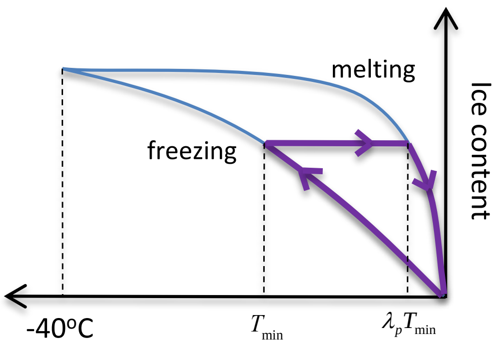

Fig. 2 Freezing and melting curve used in the analysis

If the temperature reaches the lowest value T_{min} and then is heated, the melting temperature of existing ice can be approximated as $\lambda_p T_{min}$ (Fig. 2). Thus, the melting curve should be adjusted according to the lowest temperature as:

$$S_{C_m} = \begin{cases} -5\times10^{-6}T_{min}^{\ 3} - 6\times10^{-4}T_{min}^{\ 2} - 0.0262T_{min} & (T_{min} < T < \lambda T_{min}) \\ \dfrac{0.449T}{T-2.525} & (\lambda T_{min} < T < 0^{\circ}\mathrm{C}) \end{cases} \tag{9}$$

It is true that curve fitting of ice formation might seem too simplified to catch pore structure effects of different types of concrete, so we compared the outcome of Eqs. (4)-(9) to the data from experiments and thermodynamic models. These data were the DSC ice formation data on *w/c* = 0.55 mortar [15], the ice formation model with comparison to *w/c* = 0.35 – 0.65 [17] and the low temperature calorimetry data on concrete with *w/b* = 0.40 with 0 and 5 % silica fume and *w/b* = 0.35 with 8 % silica [18]. We find that our model gives very reasonable results. Furthermore, pore sizes calculated with the latter data were also found to correspond well to Mercury Intrusion Porosimetry (MIP) data measured on the specimens from the same concretes. The type of function we are using is well-known for description of pore-structure dependent properties, see for example [19], be it permeability, water sorption, MIP or ice formation. Finally, even if the ice amount is overestimated (for example, twice), the final hydraulic induced flow may also be around double, but the cryosuction induced flow will not be affected. Thus, this overestimation has relatively small impact to the final results. (The most sensitive factor is the permeability).

2.1.3 Permeability

It is thinkable that the permeability of the transport zone in front of a propagating, homogeneous, ice front in the pore system is unaffected by ice formation. However, it is also very likely that ice formation will affect permeability, particularly during melting or heterogeneous nucleation. The permeability of unsaturated porous material has been well described by the van Genuchten equations [20] as:

$$k_r = \frac{k}{k_0} = S_L^{\ 0.5}[1-(1-S_L^{\ \frac{1}{m}})^m]^2 \tag{10}$$

$$S_L = [1+(\frac{P}{P_0})^{1/(1-m)}]^{-m} \tag{11}$$

where k_0 is the permeability of a fully saturated material (m^2), k is the permeability at a liquid saturation degree of S_L, k_r is the relative value of the reduction effect. m is determined using Eq. (11), in which the liquid saturation S_L can be experimentally measured as a function of capillary pressure P/P_0 (or capillary suction) at room temperature. Although van Genuchten's equations were originally developed for soil media and also for the vapor-liquid system, it is feasible to use those equations to describe the cement-based materials and also the effect of ice formation. It should be clarified that in a highly saturated material the air-liquid meniscus (or air-liquid interface) is almost flat at room temperature so that the capillary pressure P/P_0 becomes close to atmospheric pressure. At freezing with high degree of saturation, on the other hand, the meniscus (or interface) liquid-ice will cause suction (cryosuction) in the unfrozen part of the pore water. It also has been discussed that the permeability mainly depends on the liquid saturation, which means that no matter if the larger pores are occupied by gas or ice crystal or both, they have similar effect on the permeability of liquid water. A more practical expression for cement-based material was given by Coussy [13] as:

$$S_L = [1+(\frac{R_*}{R})^{1/(1-m)}]^{-m} \tag{12}$$

where R is the critical pore size for freezing under different temperatures, R_*=4.26nm in Coussy's paper, which reflects the characteristics of the pore size distribution and connection of cementitious materials. The parameter m represents the pore size distribution concentration, the pores are more concentrated with larger value of m [21]. For CBM, it has been verified through capillary experiments that m usually varies from 0.42 to 0.57 [22]. Here the value of m is determined according to Sun's DSC data [16], which equals to 0.5 (Fig. 3(a)). Therefore, the relative permeability by liquid saturation should be:

$$k_r = \frac{k}{k_0} = S_L^{\ 0.5}[1-(1-S_L^{\ 2})^{0.5}]^2 \tag{13}$$

In this model, the minimum temperature is chosen as -18°C, which corresponds to an ice content of 0.31. From Eq. (5), the relative permeability could reach 0.064 of the original value. Of course, this effect on permeability by freezing is hard to verify experimentally for water. The effect (≈ 1 : 16) is, however, similar to the effect of freezing on gas permeability measured by Hanaor [23] on partly and highly saturated concrete specimens with $w/c \approx 0.4 - 0.7$ which are the best measurements to our knowledge on effect of freezing on concrete permeability .

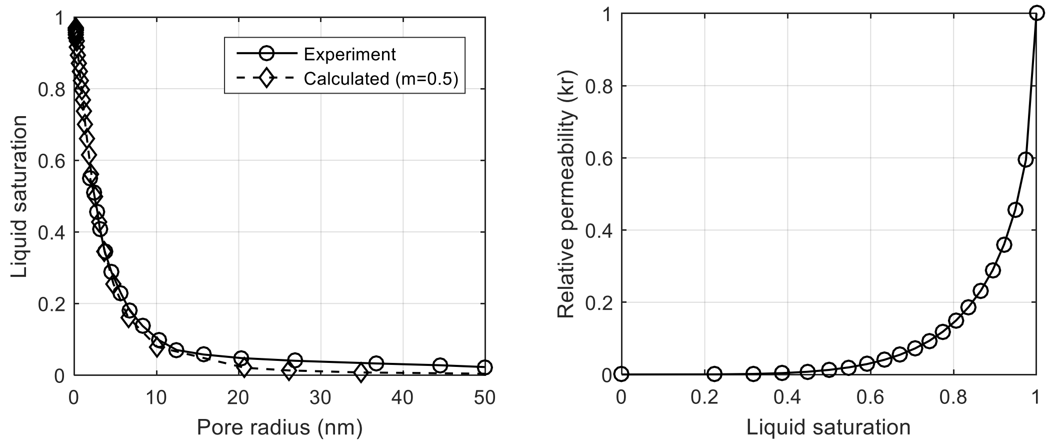

(a) (b)

Fig. 3 (a) Determination of parameter m (b) Relative permeability to liquid saturation degree

2.2 Internal pore pressures

The pore pressure induced by ice formation is composed of three parts: the hydraulic pressure (p_{hydrau}) due to ice volume expansion [24], the crystallization (p_{cryst}) and cryosuction (p_{cryo}) pressures due to the thermodynamic equilibrium between ice crystal and unfrozen water [15, 25]. As shown in Fig. 4, the hydraulic pressure depends on the increased volume when ice forms, furthermore, the increased volume which can contribute to the volume expansion is also depending on the saturation degree and amount of entrained air. Finally, the crystallization and cryosuction pressures mainly rely on the temperature and pore size due to thermodynamic equilibrium [11].

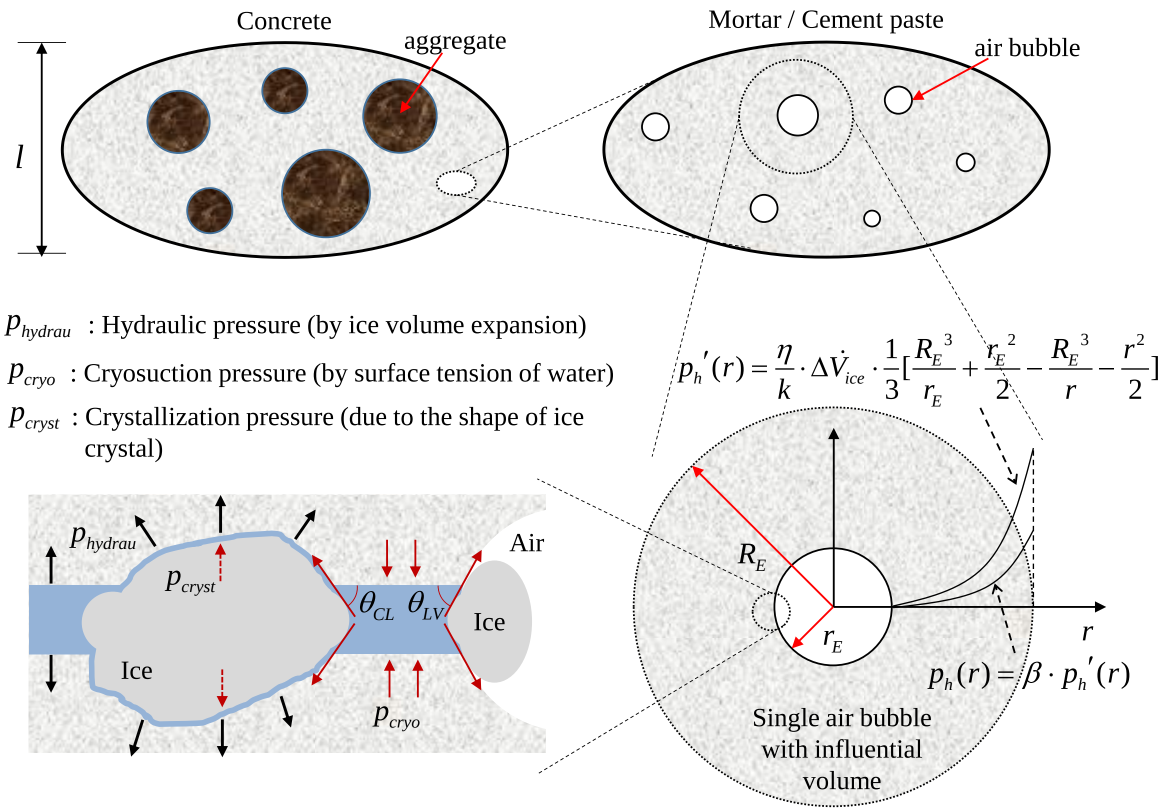

Fig. 4 Freezing induced pore pressures at different scales

2.2.1 Hydraulic pressure

There are two main hydraulic theories for the freezing process in porous cement-based materials. One is proposed by Powers [24], which aims to determine the suitable spacing factor of the air bubbles to avoid frost damage in the concrete. In his model, it was assumed that liquid water can be expelled into the entrained air voids once ice forms in the surrounding material. According to Darcy's law, a pressure gradient is a must to drive such kind of water flow, thus hydraulic pressure generates as:

$$p_h'(r) = \frac{\eta}{k}\cdot 0.09\phi\dot{S}_C\cdot\frac{1}{3}[\frac{R_E^3}{r_E}+\frac{r_E^2}{2}-\frac{R_E^3}{r}-\frac{r^2}{2}] \qquad (14)$$

where $p_h'(r)$ is the local hydraulic pressure relying on the distance (r) from the air bubbles, η is the viscosity of liquid water (Pa·s), $0.09\phi\dot{S}_C = \Delta\dot{V}_{ice}$ is the volume increasing rate when liquid water freezes, ϕ is the volume fraction of pore space, S_C is the normalized ice content, r_E and R_E are the equivalent radii of entrained air and its influential volume, respectively, as shown in Fig. 4.

Following Powers' model, Coussy and Monteiro [25] ignored the water flow, and proposed a poromechanical model for saturated porous materials, in which the increased volume can be balanced by the compression of water and ice giving liquid pressure as [25]:

$$\bar{p}_h' \approx 0.09\cdot\frac{S_C}{S_C/K_C+S_L/K_L} \qquad (15)$$

where S_L=1-S_C is the liquid water content when the material is fully saturated. K_C and K_L are the bulk moduli of the ice and liquid, respectively. This model also describes an ideal condition, which is based on the assumption that the hydraulic pressure resulting from the volume change cannot escape (sealed condition or the air voids are very far apart). It resembles the "closed container freezing" model by Fagerlund [26] that accounted for elastic deformation based on Timoshenko and Goodiers elastic analysis without considering poromechanics.

However, in reality, both water flow and self-compression will exist depending on the distribution of empty pores (like entrained air) and permeability of the materials, thus, a more comprehensive expression would be:

$$0.09\phi S_C - Q = \varepsilon_p - \phi S_C \varepsilon_C - \phi S_L \varepsilon_L \tag{16}$$

where Q (dimensionless) represents the volume of local water flow into the air bubble in Powers' model, which only accounts for part of the increased volume; ϕ is porosity and ε is the volume strain with subscripts p, C and L for porous body, ice (crystal) and water (liquid) respectively. The other part is balanced by the deformation of materials and water (liquid and solid). In Eq. (16), if the poromechanical deformation is not considered, then Q=ΔV_{ice} and the corresponding pressure distribution ($p_h'(r)$) should follow Eq. (14), as also shown in Fig. 4. However, if the local flow volume Q only accounts for part of increased volume (Q=$\beta\Delta V_{ice}$, 0<β<1), and if simply assuming the driving force of this Q still obeys the distribution in Eq. (14), then the modified hydraulic pressure should be:

$$p_h(r) = \frac{\eta}{k}\cdot\beta\cdot 0.09\phi\dot{S}_C\cdot\frac{1}{3}\left[\frac{R_E^{\,3}}{r_E}+\frac{r_E^{\,2}}{2}-\frac{R_E^{\,3}}{r}-\frac{r^2}{2}\right] \tag{17}$$

At the same time, the left part of increased volume (1-β)ΔV_{ice} is consumed by poromechanical deformation of each component (skeleton, unfrozen water and ice) under the pressure of $p_h(r)$. Here assuming a linear poroelastic behavior for each component, then within the RVE shown in Fig. 4, the total volume changes (right part of Eq. (16)) can be calculated as:

$$\varepsilon_p - \phi S_C\varepsilon_C - \phi S_L\varepsilon_L = \left(\frac{b}{K_p}+\frac{\phi S_C}{K_C}+\frac{\phi S_L}{K_L}\right)\cdot\bar{p}_h \tag{18}$$

where b=2ϕ/(1+ϕ) is the Biot coefficient [15], $\bar{p}_h$ is the volumetric average of $p_h(r)$ within the influential volume:

$$\bar{p}_h = \langle p_h(r)\rangle_V = \frac{\int_{r_E}^{R_E} p_h(r)\cdot 4\pi r^2 dr}{\int_{r_E}^{R_E} 4\pi r^2 dx} = \frac{\eta}{k}\cdot\beta\cdot 0.03\phi\dot{S}_C\cdot\frac{R_E^{\,6}-1.8R_E^{\,5}r_E+R_E^{\,3}r_E^{\,3}-0.2r_E^{\,6}}{R_E^{\,3}r_E-r_E^{\,4}} \tag{19}$$

On the other hand, the local water flow q (m/s) into the central void is:

$$q = q(r_E) = \frac{1}{4\pi r_E^{\,2}}\cdot\beta\cdot 0.09\phi\dot{S}_C\cdot\frac{4}{3}\pi(R_E^{\,3}-r_E^{\,3}) = \beta\cdot 0.03\phi\dot{S}_C\cdot\frac{R_E^{\,3}-r_E^{\,3}}{r_E^{\,2}} \tag{20}$$

Combining Eqs. (19) and (20), the water flow into the central void regarding the average pressure becomes:

$$q = \frac{(R_E^{\,3}-r_E^{\,3})^2}{(R_E^{\,6}-1.8R_E^{\,5}r_E+R_E^{\,3}r_E^{\,3}-0.2r_E^{\,6})r_E}\cdot\frac{k}{\eta}\bar{p}_h \tag{21}$$

After differentiation of Eq. (16) with respect to time, the following equation is derived:

$$\begin{aligned}0.09\phi\dot{S}_C - \frac{A_E}{V_E}\cdot q &= \dot{\varepsilon}_p - \phi\frac{\partial(S_C\varepsilon_C)}{\partial t} - \phi\frac{\partial(S_L\varepsilon_L)}{\partial t}\\ &= \dot{\varepsilon}_p - \phi S_C\dot{\varepsilon}_C - \phi\dot{S}_C\varepsilon_C - \phi S_L\dot{\varepsilon}_L - \phi\dot{S}_L\varepsilon_L\end{aligned} \tag{22}$$

Considering $\dot{S}_C = -\dot{S}_L$, Eq. (22) can be written as:

$$(0.09+\varepsilon_C-\varepsilon_L)\phi\dot{S}_C-\frac{A_E}{V_E}\cdot q=\dot{\varepsilon}_p-\phi S_C\dot{\varepsilon}_C-\phi S_L\dot{\varepsilon}_L \tag{23}$$

Still Eq. (23) can be further simplified as:

$$0.09\phi\dot{S}_C-\frac{A_E}{V_E}\cdot q=\dot{\varepsilon}_p-\phi S_C\dot{\varepsilon}_C-\phi S_L\dot{\varepsilon}_L \tag{24}$$

Because (ε_C-ε_L) = $\bar{p}_h(1/K_C-1/K_L)$, and if $\bar{p}_h$ ranges from 10Mpa to 50Mpa, (ε_C-ε_L) is between -0.0034 and -0.017. In reality, considering the tensile strength and plasticity of CBM, $\bar{p}_h$ should probably not exceed 20Mpa. In Eq. (24), A_E=4πr_E^2, V_E=4/3πR_E^3; r_E and R_E are the equivalent radii of the entrained air (or the empty pores) and the influential volume, which should satisfy:

$$\frac{r_E^{\ 3}}{R_E^{\ 3}}=\phi_{air} \tag{25}$$

where ϕ_{air} is the air content of CBM and r_E can be determined by the following formula:

$$r_E=\langle r\rangle_{V_{air}}=\frac{\int r\cdot v(r)dr}{\phi_{air}} \tag{26}$$

where $v(r)$ is the size distribution of entrained and entrapped air, which can be determined by empirical equations [27, 28] or experimental measurements [29, 30]. Finally, substitute Eqs. (18) and (21) into Eq. (24), the governing equation of the hydraulic pore pressure becomes:

$$0.09\phi\dot{S}_C-\frac{3r_E(R_E^{\ 3}-r_E^{\ 3})^2}{(R_E^{\ 6}-1.8R_E^{\ 5}r_E+R_E^{\ 3}r_E^{\ 3}-0.2r_E^{\ 6})R_E^{\ 3}}\cdot\frac{k}{\eta}\bar{p}_h=\left(\frac{b}{K_p}+\frac{\phi S_C}{K_C}+\frac{\phi S_L}{K_L}\right)\cdot\dot{\bar{p}}_h \tag{27}$$

In the above equation, the viscosity of liquid water (η) depends on the temperature, which can be calculated as [13]:

$$\eta=2.88\times10^{-5}\exp(\frac{509.53}{123.15+T}) \tag{28}$$

Then by solving Eq. (27), local average value of hydraulic pore pressure ($\bar{p}_h$) can be obtained at each location and time.

2.2.2 Negative capillary pressure by cryosuction

As mentioned above, due to the surface tension, there is a pressure difference between liquid and crystal on the crystal/liquid interface, and also a difference between liquid and gas on the liquid/vapor interface. In a highly saturated system at room temperature the capillary pressure under the liquid/vapor interface $P/P_0\approx$ atmospheric pressure and the meniscus between water and air is flat. At freezing of such a highly saturated cement-based material the capillary pressure is always negative. Depending on the liquid saturation degree, the pressure in the liquid phase at freezing can be deduced more accurately from the surface tension of crystal/liquid interface and liquid/vapor interface:

$$\kappa_{CL}\gamma_{CL}=\kappa_{LV}\gamma_{LV} \tag{29}$$

where κ_{LV} and γ_{LV} represent the curvature and surface energy of liquid/vapor interface respectively. Then, the cryosuction pressure can be related to the freezing point by [15]:

$$p_l=-\kappa_{LV}\gamma_{LV}=\Delta S_{fv}(T-T_0) \tag{30}$$

It should be noticed that the cryosuction pressure calculated by Eq. (30) (-12 MPa at -10°C and -24 MPa at -20°C) can easily exceed the tensile strength of conventional water, say, -0.5 MPa [31]. In fact, the water in nano-/meso pores should not be treated as conventional water both because of the thermodynamic equilibrium and the confinement by pore wall (see Appendix B).

Here also we assume that capillaries/mesopores/gel pores are saturated whereas air voids are empty or partially empty at start of freezing so the interface liquid/vapour or ice/vapour will be at the wall of air pores whereas interface ice/liquid will be in the saturated paste or with the ice crystal growing from an air void that is, at least, partially empty.

3. Global water transport

Once there is a temperature gradient (calculated by Eqs. (1-2)), the ice content and permeability would be different at each time and location (x,t). Then the hydraulic pressure calculated by Eq. (25) and the cryosuction pressure by Eq. (28) will also be non-uniform. Therefore, other than the local flow q (m/s) into and out of the empty voids, a global flow g (m/s) will also be generated due to the global pressure gradient in x direction, see Fig. 5. Here, although the hydraulic pressure at micro/meso scale is not uniformly distributed, the average value ($\bar{p}_h$) can be used to calculate the global flow at a larger scale. The water uptake measured in the experiments is then mainly due to the global flow.

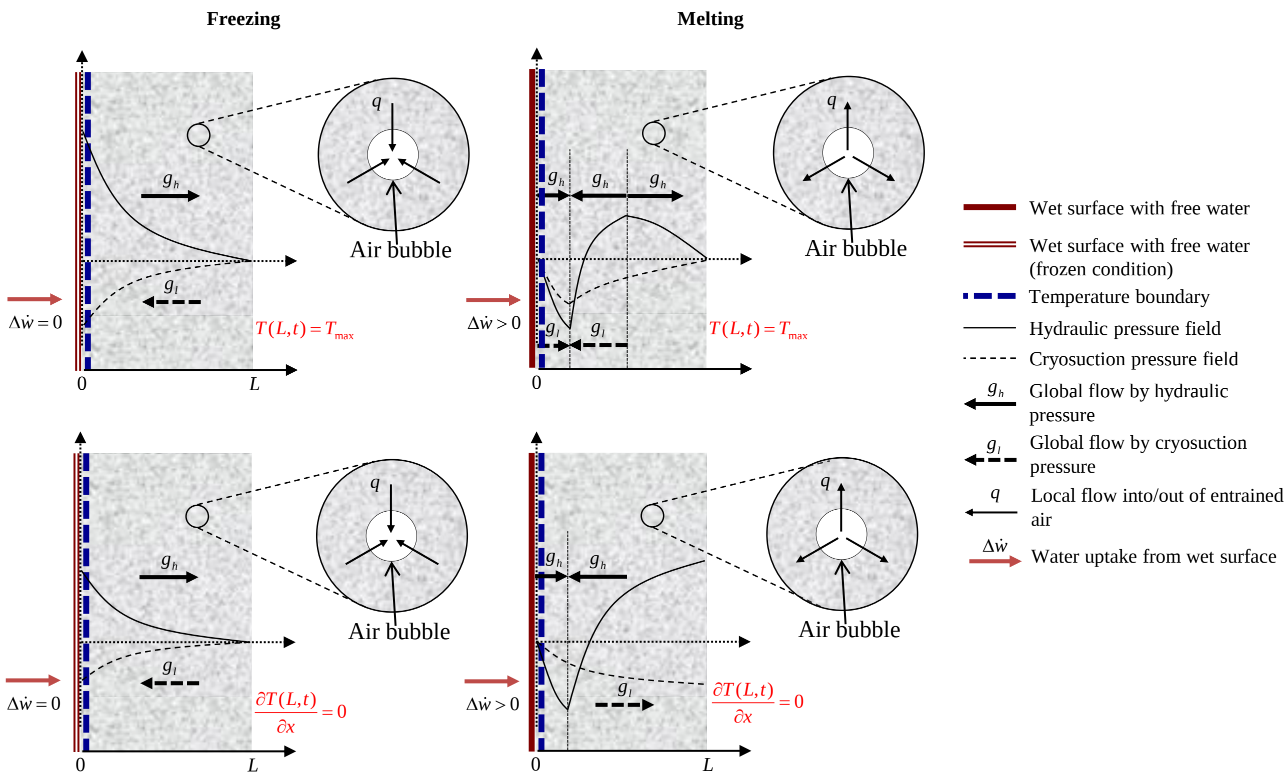

Fig. 5 Local flow to empty voids by hydraulic pressure and global flow in x direction by global pressure gradient

The directions of the flows by each kind of pressure are shown in Fig. 5. During freezing, part of the increased volume due to ice formation can be consumed by entrained or entrapped air, thus the hydraulic pressure can be reduced but not eliminated. During this process, the global hydraulic pressure will drive flow inward while the cryosuction pressure gradient will drive the flow outward. During the heating period, assuming melting progresses from a warmer and wet surface, both cryosuction and hydraulic pressure gradient should cause inward flow near the wet surface.

Here the specimen is assumed fully saturated with some entrained or entrapped air staying empty, but for many cases in reality, fully saturated condition just happens within a certain depth from the wet surface, which was termed as "depth of saturation" [24]. In Powers' model, the depth of saturation is essential to the magnitude of hydraulic pressure because the liquid was assumed not compressible, and the critical depth where the material strength is surpassed is usually within a few millimeters. If applying Powers' model to Fig. 5, the calculated value would reach hundreds of mega Pascals. Then it is more proper to consider the liquid and ice as compressible in this paper. Therefore, the global pressure gradient is determined mainly from local pressure at different depths at a smaller scale, and the depth of saturation is not essential for the cases discussed here. Then the global water flow $g(x,t)$ (m/s) at each time and depth can be calculated as:

$$g(x,t) = -\frac{k(x,t)}{\eta(x,t)}\left(\alpha\frac{\partial \overline{p}_h(x,t)}{\partial x} + (1-\alpha)\frac{\partial p_l(x,t)}{\partial x}\right) \tag{31}$$

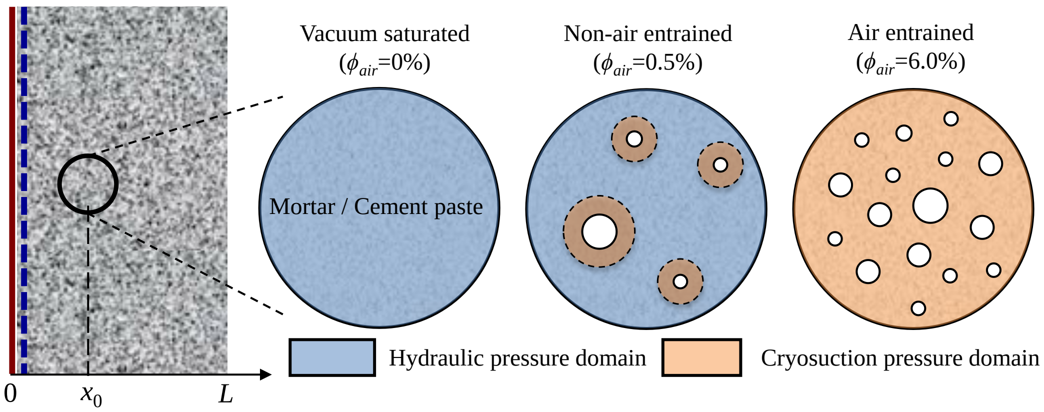

Fig. 6 Proportion of hydraulic and cryosuction pressures affected by air content

In Eq. (31), the factor α represents the proportion of volume where the hydraulic pressure or cryosuction pressure dominates, which depends on the volume and size of the entrained/entrapped air bubbles (see Fig. 6). It is known that as the amount of entrained air increases, the total pore pressure will decrease from positive to negative continuously [15], and usually 6% entrained air may totally avoid the hydraulic pressure. There are models on how the air void system affects the total pore pressure [32, 33]. But here α is roughly assumed as α=1-ϕ_{air}/0.06 ($0 \leqslant \alpha \leqslant 1$), for the simplicity of modeling work.

In real condition, once the wet surface is frozen, the water uptake or water flow at the wet surface will stop. If using Heaviside step function $H(x)$ to describe the effect of frozen wet surface, the speed of water uptake ($\Delta \dot{w}$) from the wet surface (or global flow at x=0) becomes:

$$\Delta \dot{w} = g(0,t)\cdot H(T(0,t)) \tag{32}$$

where,

$$H(x) = \begin{cases} 0, & x < 0 \\ 1, & x \geq 0 \end{cases} \tag{33}$$

Finally, the total amount of water flow into CBM during wet frost exposure is:

$$\Delta w = \int g(0,t)\cdot H(T(0,t))\, dt \tag{34}$$

4. Simulation and experimental data

The temperature history is mutually controlled at the wet surface, and two types of temperature boundary are simulated and discussed for the opposite surface, that is, the heat-insulated (second-type) boundary, and the constant temperature (first-type) boundary. Although in the lab test such as ASTM 666C Proc. A, SS 137244 and CDF/CIF, the uncontrolled temperature surface is not exactly insulated, so the heat exchange with the surrounding air is rather negligible compared to the heat transfer inside the concrete. For the general analysis of temperature, pressure and water flow, some typical parameters are chosen (Table 1 and Table 2). But some parameters might be changed when comparing the particular experimental data.

Table 1. Material properties used in the model

Lowest temperature T_{min}	-18 ^oC
Highest temperature T_{max}	4 ^oC
Thickness L	50mm
Saturated permeability k_0 (undamaged)	$10^{-21}m^2$
Void ratio (total porosity)	0.15
Bulk modulus of porous body K_p	13.9 GPa
Bulk modulus of ice crystal K_C	8.8 GPa
Bulk modulus of liquid water K_L	2.2 GPa

Table 2. Equivalent radii and spacing factors

	Air content	r_E	R_E	$\bar{L}$ $=R_E- r_E$
Vacuum saturated	0	-	Inf.	Inf.
Non-air entrained	0.5%	0.8×10^{-4}m	8.1×10^{-4}m	7.3×10^{-4}m
6% air entrained	6%	0.8×10^{-4}m	3.8×10^{-4}m	3.0×10^{-4}m

In Table 2, the effect of entrapped and entrained air is considered in the hydraulic model. The representative radii (r_E) of empty pores are based on the empirical pore size for non-air entrained [28] and 6% air entrained concrete [29]. Following the definition by Powers [24], the spacing factor ($\bar{L}$) is the distance between the surface of an air bubble to its sphere of influence. The estimated values in Table 2 are close to the image analysis by Fonseca and Scherer [30], in which $\bar{L}$=727μm when ϕ_{air} =0.43% and $\bar{L}$=388μm when ϕ_{air} =5.58%. Past experiments also show that the normalized size distributions of air bubbles are quite similar regardless of the total air content [29, 30], therefore, it is convenient and reasonable to choose a representative value of r_E for all the cases in Table 2.

4.1 Temperature gradient

In Fig. 7, dx means the depth from the temperature surface inwards. Fig. 7 (a) and (b) show the temperature and temperature gradient of heat insulated boundary condition. Since the thickness of the material is quite small, the temperature on the other side can follow the controlled one quickly, and almost reach the lowest temperature through the freeze/thaw cycle. It can be seen that the temperature gradient reaches the highest value at the wet surface and decreases as depth becomes bigger. The temperature gradient at each depth also always changes, and it is difficult to find even a short period with a constant temperature gradient. Fig. 7 (c) and (d) present the same information but with constant temperature on the uncontrolled surface. It can be seen that when the temperature reaches minimum value and is kept constant, a constant temperature gradient can also be created along the depth. Actually, many wet frost exposure tests are conducted with one or more heat insulated boundaries, but according to the figures above, the constant temperature boundary might be a better choice to provide a stable and uniform temperature gradient.

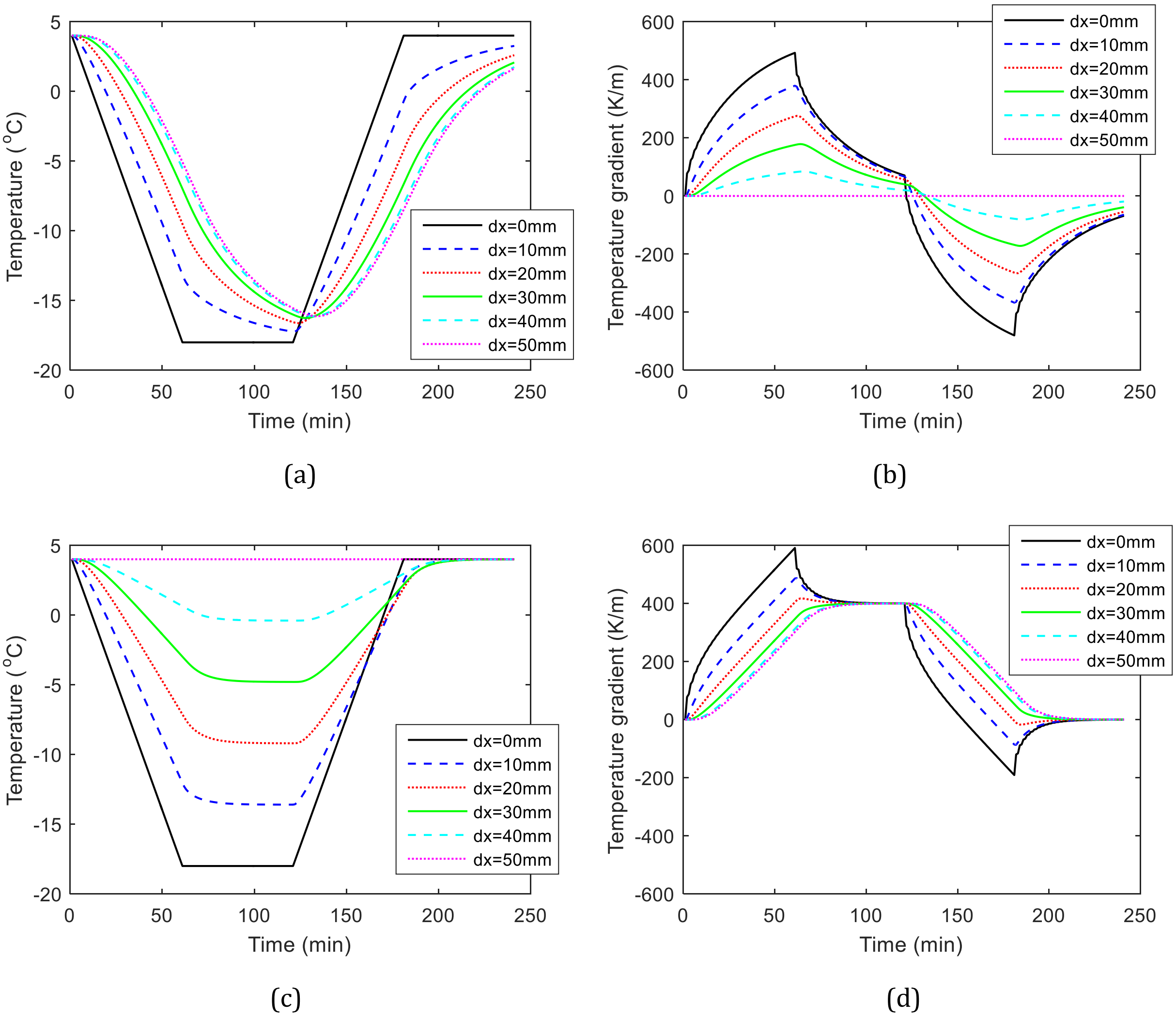

Fig. 7 Temperature distribution and gradient. (a) and (b): heat insulated boundary; (c) and (d) constant temperature boundary

4.2 Pressure distribution

The hydraulic pressures and suction that may arise due to the increasing and decreasing ice formation have been calculated. Figs. 8 and 9 show plots of resulting pressure and suction during the freezing and thawing.

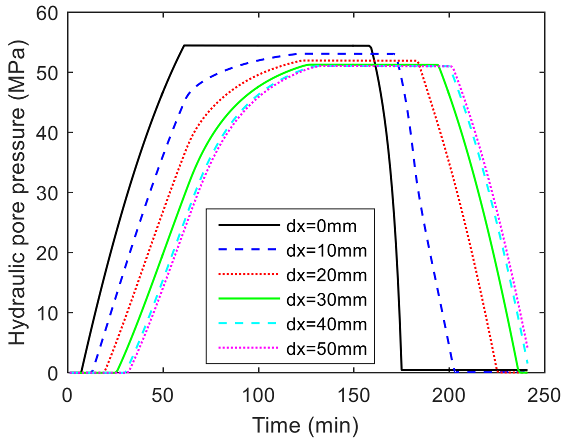

(a)

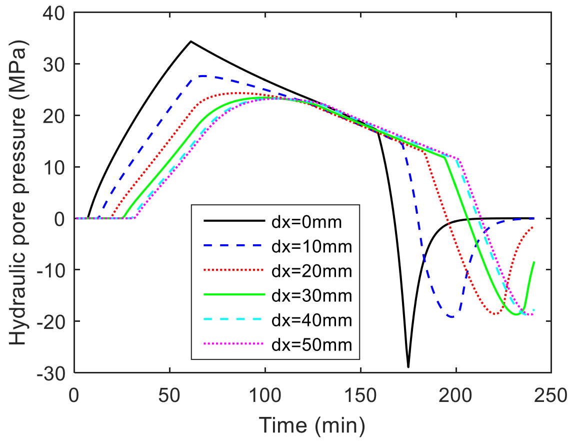

(b)

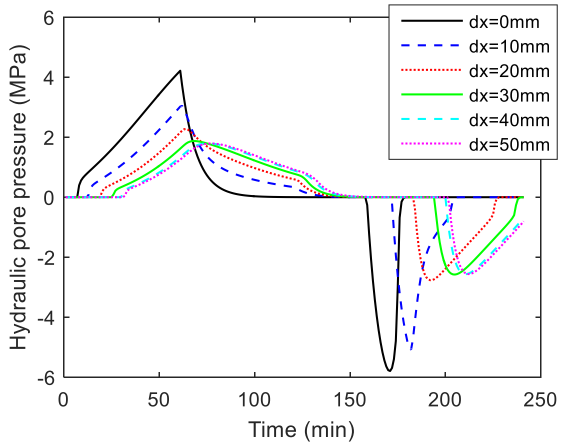

(c)

Fig. 8 Hydraulic pressure in pores for different air content (a) Ideal fully saturated (b) Water saturated non-air entrained concrete (ϕ_{air}=0.5%) (c) Water saturated 6% air entrained concrete

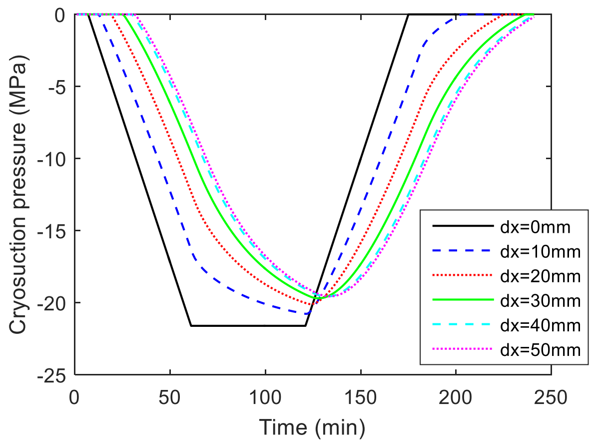

Fig. 9 Cryosuction pressure in pores

Still dx in Figs. 8 and 9 means the depth from controlled temperature and wet surface. Fig. 8 shows the effect of air bubbles on the hydraulic pressure, which agrees with common experiment observation: highest expansion under vacuum saturation; less expansion for water saturated non-air entrained concrete; and no expansion (but contraction due to cryosuction) if 6% air is entrained [15]. Fig. 8 (a) just attempts to show an ideal condition based on the linear elastic assumption (in order to reduce the complexity of modelling). However, under real experimental or in site situations, the "vacuum saturation" is not likely to happen. The very high suction in Fig.8 (b) is similar to what can be deduced during normal drying of concrete and is discussed further in Appendix B. The permeability ($10^{-21}m^2$) chosen for the undamaged CBM is actually a lower bound of the previous measurements [34, 35], which leads to a bit overestimation of the hydraulic pore pressure. For example, the water saturated non-air entrained concrete (Fig. 8 (b)) may have an initial pore pressure of 30-40 MPa which will surely cause some damage (plastic expansion) and enlarge the permeability, so that the pore pressure can be reduced and limited within the material's strength [36, 37]. The sensitivity of permeability on the water transport will be discussed later. The cryosuction pressure is mainly depending on the size distribution of small pores (r=100nm corresponds to -0.8MPa), which are not affected by the amount of air bubbles. The calculated cryosuction pressure distribution can be seen in Fig. 9, which is linear to the temperature distribution.

4.3 Water flow and comparison

Based on the pressure distribution in the previous section, the global water flow at each time and different depth is shown in Fig. 10. According to Fig. 7 (b), the closer to the controlled temperature surface, the bigger temperature gradient can be generated, and results in a bigger pressure gradient. Therefore, the water flow by both hydraulic and cryosuction pressure shows a gradual decrease as the depth increases, either inward flow (positive) or outward flow (negative). It should be noticed that if the wet surface is attached with pure water, which may freeze to ice first when temperature drops, the water flow at the wet surface will be cut, as the black line (dx=0) shown in Fig. 10 (a) and (b). When the wet surface melts during thawing process, there would be a rapid water uptake from the wet surface, resulting from the sudden melting of ice near the surface. This rapid water flow by hydraulic pore pressure also resembles the pumping effect in the "Micro-Ice-Lens Model" [38]. In order to make the model concept clearer and easier, the global flow at macro scale and the driving forces (pore pressures) in micro (meso) scale are treated at different scales and independent with each other. It may cause another problem that the global water flow may not be continuous ($\partial g(x,t)/\partial x \neq 0$), so that different depths may have different net change in water amount after one freeze/thaw cycle. As a result, the redistribution of water content occurs, but finally an equilibrium moisture distribution should be achieved slowly inside the material. When the material is already water saturated, the additional absorbed water may either fill the cracks by frost damage (non-air entrained CBM) or fill the entrained air voids (air entrained CBM), and as the number of cycles increases, the damage will also become more and more serious. This process also agrees with the experimental phenomena that the frost damage and absorption will cumulate with the number of freeze/thaw cycles [2, 39, 40].

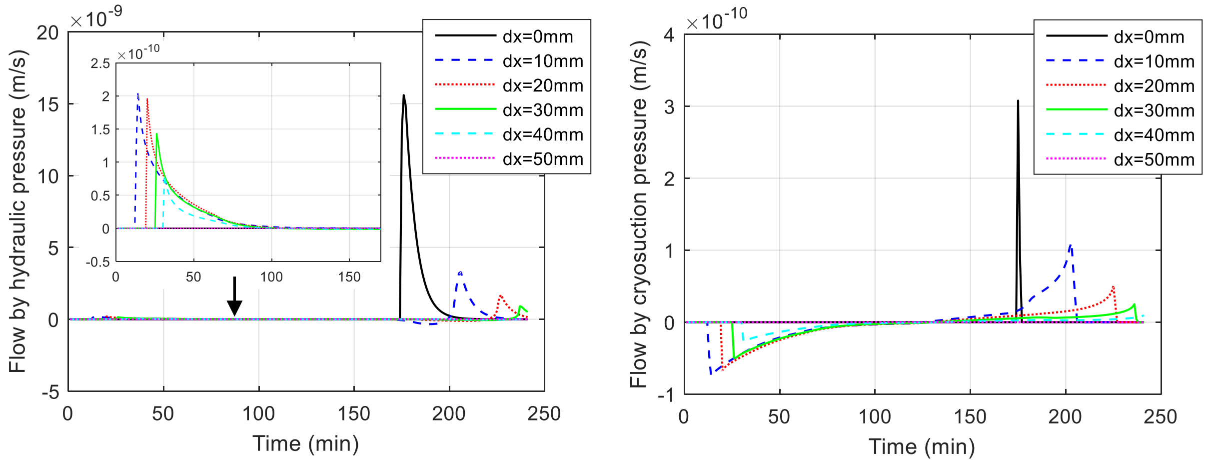

(a) (b)

Fig. 10 The water flow inside CBM at different location and time. (a) Hydraulic pressure induced flow (ϕ_{air}=0.5%); (b) Cryosuction pressure induced flow (ϕ_{air}=6.0%)

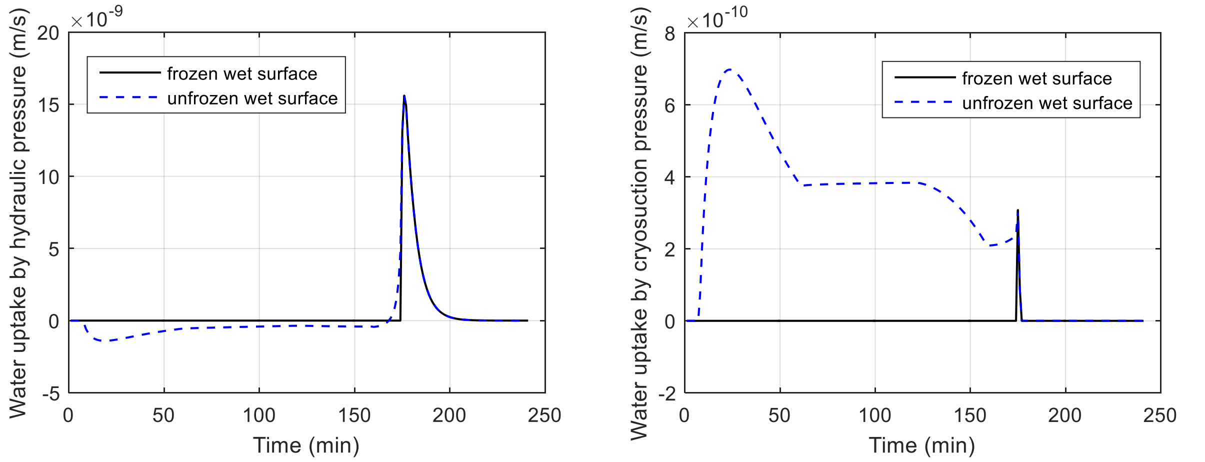

(a) (b)

Fig. 11 Water uptake (speed) from the wet surface with and without considering blocking ice at surface. (a) Hydraulic pressure induced uptake (ϕ_{air}=0.5%); (b) Cryosuction pressure induced uptake (ϕ_{air}=6.0%)

The water flow at the wet surface in Fig. 10 is actually the water uptake of the whole material, which is shown in Fig. 11 together with the case of unfrozen boundary condition. If the wet surface is always unfrozen (for example high concentration solution is used), during freezing, cryosuction pressure will drive water from wet surface inward, while the hydraulic flow is in opposite direction; but during melting, both the two pressures will drive water inward. In most of the real cases, a wet surface cannot stay unfrozen, and flow only exists before a wet surface freezes or after it melts, i.e. only a very short period of flow through the surface.

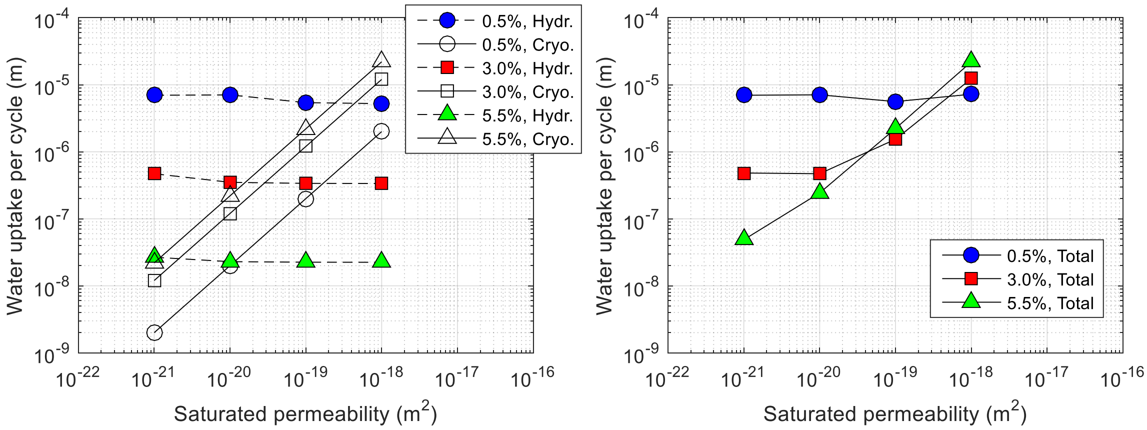

Fig. 12 Total amount of water uptake per cycle with different air content and permeability

As mentioned before, the permeability chosen for the above simulation is a lower bound, and in the real condition, the permeability may vary according to a number of factors (mix proportion, age, admixture and so on), and it can also be enlarged significantly if frost damage occurs [12]. Therefore, the sensitivity of permeability under saturated condition is analyzed in Fig. 12. From which it can be seen that the total water flowing into the material by the hydraulic pressure mainly relies on the amount of entrained/entrapped air, because the magnitudes of hydraulic pressure are quite different (Fig. 8). Although the hydraulic pressure will drop significantly if permeability increases (Eq. (27)), the increased permeability will also make the global flow from wet surface much quicker, thus the saturated permeability may not have big effect on the hydraulic pressure induced flow. On the contrary, the cryosuction induced flow is proportional to the permeability according to Darcy's law, because the pressure distribution mainly depends on the temperature field. In sum, the water flow by the sum of the two pressures still relies on the chosen permeability to some extent. This makes the perfect fitting with experiment data difficult, because the exact permeability of each CBM is difficult to measure, especially when the materials are damaged by frost action.

Table 3. Parameters in experiments and simulation (k_0=10^{-21}m^2)

	ϕ_{air}	$\bar{L}$ (mm)	ASTM C666A (10K/h)			SS 137244 (5K/h)		
			Q_{cal} (10^{-6} m)	g_{cal} (10^{-9} m/s)	g_{mea} (10^{-9} m/s)	Q_{cal} (10^{-6} m)	g_{cal} (10^{-9} m/s)	g_{mea} (10^{-9} m/s)
040-00*	1.6	0.99	7.35	4.4	4.5	6.22	2.9	1.9
040-05	2.0	0.97	7.08	4.4	6.8	5.77	2.7	4.0
040-05A	5.1	0.33	0.34	1.1	1.8	0.17	0.24	0.69
035-08	2.0	1.04	7.14	4.4	4.8	5.90	2.7	4.8
035-08A	7.8	0.16	0.06	0.4	2.5	0.04	0.1	0.76
035-08L	1.7	1.03	7.02	4.5	1.0	5.70	3.0	0.72
035-08Ls	1.9	1.30	9.86	3.5	2.5	12.7	3.8	3.9

*: w/c and % silica fume, A: air entrainment, L/Ls: dry and saturated light weight aggregates

In order to verify the reliability of the proposed model, some experimental data on the water flow during wet frost exposure has been collected [10], as shown in Table 3. The details of the material properties can be found in [4, 41], and here only the most important parameters are selected: the air content (ϕ_{air}) and spacing factor ($\bar{L}$). Since the spacing factors are available for the selected experimental data, the radius of sphere of influence can be achieved as $R_E = \bar{L} + r_E$. Other parameters still follow the values in Table 1, and the cooling rates for ASTM C666A and SS 137244 are set as 10K/h and 5K/h, respectively. The measured water flow (g_{mea}) is the average speed of water flow during which the wet surface stays unfrozen, so the g_{cal} in Table 3 is also calculated the same way based on the total water uptake (Q_{cal}) and duration when the surface flow happens. The comparison between calculated and measured values is shown in Fig. 13. Considering numbers of uncertainties, such as type of aggregates, effect of silica fume, permeability and damage level, and also considering the sensitivity in experimental measurements, the simulated result can catch the experiment phenomena satisfactorily.

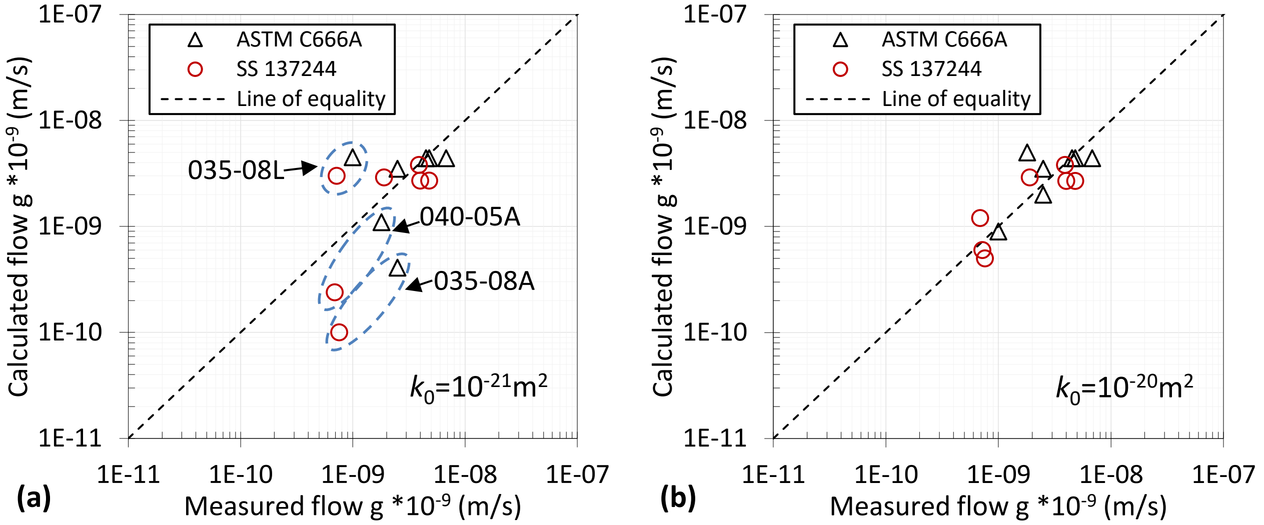

Fig. 13 Measured global flow and calculated results (a) Intrinsic permeability k_0=10^{-21}m^2, porosity of dry light-weight aggregates is ignored; (b) Intrinsic permeability k_0=10^{-20}m^2, porosity of dry light-weight aggregates is regarded as 5% entrained air.

From Table. 3 and Fig. 13 (a), it can be seen that most of the data sets are in the same magnitude and close to each other, except for the air-entrained cases (035-08A and 040-05A), of which the measured values are bigger than the calculated values. It is because that once additional air is entrained to CBM, the hydraulic pressure will be reduced significantly and the crysuction induced flow become more dominant. However, the cryosuction flow is very sensitive to the permeability, and since a lower bound value (k_0=10^{-21}m^2) is used in the above simulation, the total water uptake might be underestimated for the air-entrained cases. For the case with dry light-weight aggregates but without entrained air, the calculation overestimates the water uptake. This is mainly because the porosity of light-weight aggregates is considerably larger, which can have similar functions as the entrained air in reducing the hydraulic pressure. In sum, if adopting k_0=10^{-20}m^2, and roughly regarding 035-08L, which has 5% entrained air equivalently, the calculated water uptake becomes much closer to the measured data (Fig. 13 (b)). Nevertheless, the effects of light weight aggregates and silica fume are difficult to quantify at this moment since they may affect the moisture content and pore size distribution, which need further investigation.

5. Further discussions

5.1 Effects of cooling rate, minimum temperature and thickness

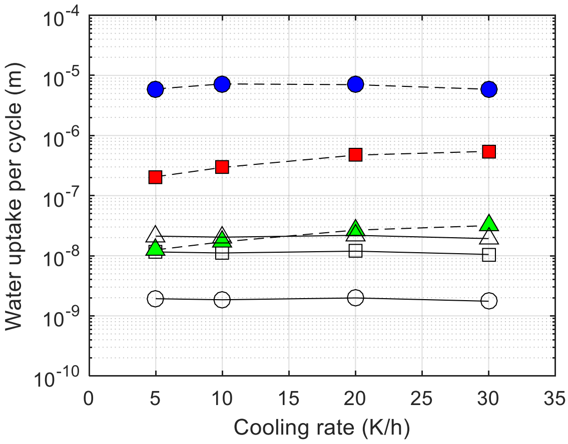

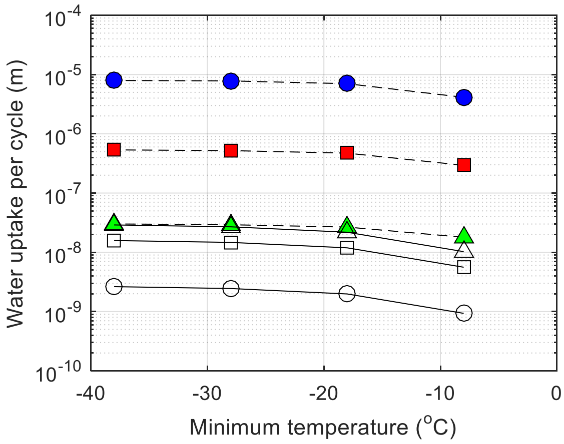

(a) (b)

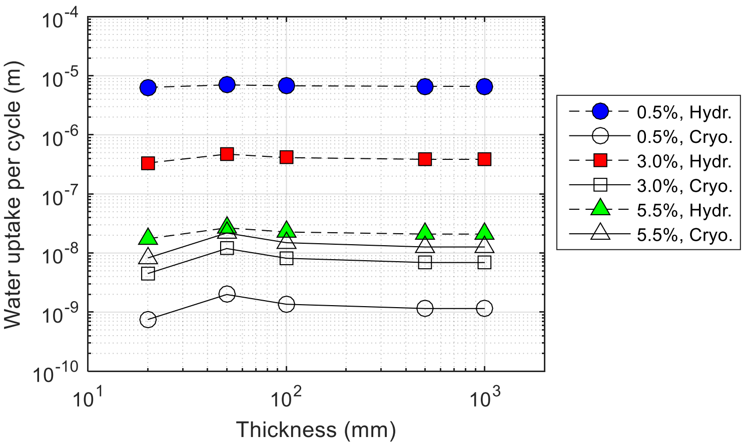

(c)

Fig. 14 Effect of parameters on the total water uptake per cycle. (a) Effect of cooling rate; (b) Effect of minimum temperature; (c) Effect of thickness

Since the proposed model has also taken several other parameters into consideration, such as the cooling rate, minimum temperature and thickness of specimen, thus the sensitivities of those variables are analyzed here, see Fig. 14. The cooling rate can affect the speed of ice formation, which is also an important factor in Power's hydraulic model and the proposed Eq. (25) in this study. Once the ice forms more rapidly, the entrained air will perform less efficiently and result in a higher hydraulic pressure and bigger pumping effect when wet surface melts. Thus, in Fig. 14 (a), the 3% and 5.5% entrained cases show a significant increment (but still within one order) in the hydraulic induced water uptake when cooling rate increases. For the cryosuction induced uptake, higher cooling rate will generate a higher temperature gradient, but at the same time, the duration of water flow becomes shorter. Thus, finally the cryosuction induced uptake is less affected by the cooling rate. In Fig. 14 (b), all the cases show an increasing uptake if the minimum temperature becomes lower. It is because both the hydraulic and cryosuction pressure will increase once more ice is formed and grows into smaller pores. The thickness seems to have less influence on the water uptake (Fig. 14 (c)), since the water flow at the wet surface is mainly controlled by the local temperature and pressure gradient near the surface. This feature also makes the proposed model more easy and convenient to be used for a quick estimation of the water uptake in lab test and real cases, because only the area of wet surface is needed regardless of the size and thickness of material.

5.2 Constant temperature boundary

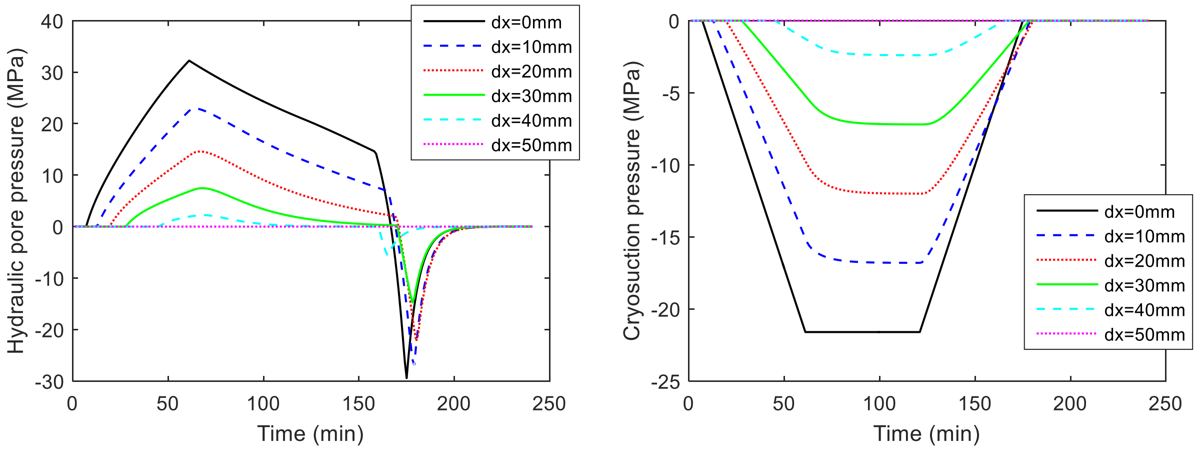

Fig. 15 Hydraulic pore pressure and cryosuction pressure distribution when constant temperature is kept on the opposite surface (20K/h). (a) Hydraulic pore pressure (ϕ_{air}=0.5%); (b) Cryosuction pressure (ϕ_{air}=6.0%)

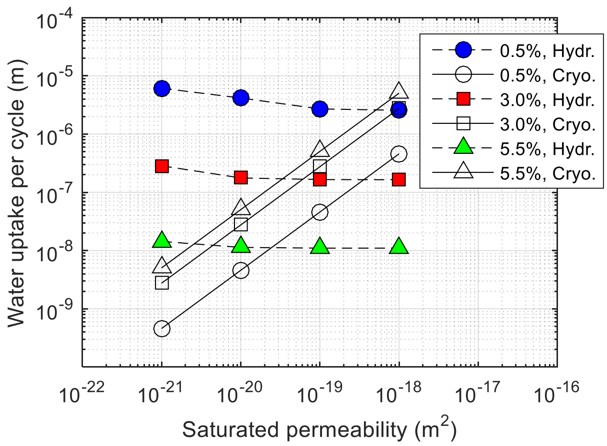

Fig. 16 The water uptake per cycle under constant temperature boundary

If the temperature is kept constant on the uncontrolled surface (opposite of wet surface), a more constant temperature gradient can be achieved, as discussed in Fig. 7. Then under this kind of condition, the hydraulic pressure as well as cryosuction pressure distribution are drawn in Fig. 15, and the total water uptake after one freeze/thaw cycle is shown in Fig. 16. It can be seen that the pressure gradients are also more stable as a result of the stabilized temperature gradient. Comparing Fig. 16 with Fig. 12, the hydraulic pressure induced uptake is close to each other, which means the pumping effect near the wet surface is almost the same. However, the water uptake by cryosuction is reduced in Fig. 16, which owes to the smaller temperature gradient during melting (see Fig. 7 (b) and (d)).

5.3 Relation to frost damage

Since the paste- (capillary-/meso-/gel-) porosity is assumed filled before start of freeze/thaw, the accumulation of water in the concrete due to the modelled mechanisms can be in the air voids and in increased pore space created by frost damage depending on the circumstances. If the air void quality and volume is either too low or partially filled by water so that its protective effect is reduced to a critical level, damage is initiated immediately. Then the water uptake will probably fill up both cracks, pore structure damage and air voids, see [17, 18]. As long as air void quality and volume are sufficient the filling of the air voids may continue for a while without damage. Further treatment of frost damage is beyond the scope of this paper and treated elsewhere.

6. Conclusions

In this study, the pressure and flow during wet frost exposure has been modeled and discussed in detail. The simulation starts from the temperature distribution, followed by the calculation of ice content, permeability change and two kinds of driving forces (hydraulic pressure and cryosuction pressure). Depending on the pressure gradients, the global water flow is calculated and the comparison with previous experiment data shows a satisfactory agreement. Finally, the effects of other variables as well as the boundary condition are discussed.

The simulation of the temperature shows that, for the current testing methods, in which an insulated temperature boundary is often used, it is difficult to obtain a constant and stable temperature gradient. Therefore, it is much better to use a constant temperature boundary, specially aiming to investigate the water flow by pressure gradient.

The hydraulic model used in this study is a combination of poromechanical laws and water movement (by Darcy's law), so that it can be applied to both non-air entrained and air entrained CBM. Both the hydraulic pressure and cryosuction pressure gradients are simulated based on the temperature field, and the reduced permeability blocked by ice. It is found that during melting, negative hydraulic pressure will arise due to the sudden volume decreasing when ice melts. This negative pressure will suck the water from wet surface inward, in accordance to the pumping effect discussed in previous research.

Finally, the global water flow induced by two driving forces are calculated, and the water uptake from wet surface is compared with measured data, which is found in a satisfactory agreement considering numbers of uncertainties and sensitivity of experiments. Results show that the water uptake by hydraulic pressure is sensitive to the entrained air: the larger air content, the smaller water uptake will be. On the contrary, the cryosuction pressure induced water flow is linear to the material's permeability. The entrained/entrapped air amount also affects the volume proportion where hydraulic pressure or cryosuction pressure dominates. Finally, the effects of other parameters are also discussed, such as the cooling rate, lowest temperature, thickness, boundary condition of the opposite surface and so on. Showing for example that uptake is mainly taking part near the surface where temperature gradients can be high.

This investigation and simulation for typical wet frost exposure can help to understand and predict the deterioration in real structures, as discussed at the beginning. Thus, more practical simulation could be conducted for real cases (like road, bridge deck and so on) based on this work.

Acknowledgements

The work was mainly done while the authors were visiting Professor George Scherer at Princeton in 2013 whom we thank for accommodation, sharing of knowledge and fruitful discussions. Besides, the first author would like to thank for the Cross-ministerial Strategic Innovation Promotion Program (SIP) granted by Japan Science and Technology Agency. SJ also thanks the Norwegian University of Science and Technology for granting a sabbatical.

Appendix A. Simplification of heat release of freezing and mismatch in thermal strain

First assuming that typical normal density concretes have capillary + gel porosity in the order of 12% (paste volume fraction in the order of 28-35% and paste porosity in the order of 35-45 % by paste volume, then, giving variation in the total porosity from 10% to 16%). This excludes the air voids that could be assumed empty before filled temporarily during freeze/thaw, and also assumes non-porous aggregate. Then 12% by volume is around 5% by mass for a normal density concrete. If the degree of saturation is approximately 100%, 25% freezable water (at -20°C) should make up in the order of 1% freezable water by weight of the concrete. For 1 kg concrete this gives a latent heat of 10g × 334 J/g = 3.34 kJ at phase change (which is a state function and thus can be assumed valid for the whole phase change from, say 0 to -20°C and back again to zero). On the other hand, the heat needed to cool this concrete body of 1 kg from, say +20 to -20°C is much larger. The heat capacity of concrete is in the order of 1 kJ/kg·K requiring a heat of around 1 kJ/kg·K × 40 K = 40 kJ/kg concrete. Therefore, even though the heat capacity of concrete is affected a bit by moisture content and whatever phase the water is in (water has a very high heat capacity of 4.2 kJ/kg·K and 2.05 kJ/kg·K for ice) the heat contribution of phase change of this typical concrete frozen from 20 to -20°C is approximately 3.34/40 = 8.4% < 10 %.

For the thermal contribution of different phases, first, assuming fully saturated without air-entrainment, freezing of 25% water will cause (1.09-1) ×0.12×0.25=2700μ volume expansion. At the same time from 0°C to -20°C, the difference between matrix (10×10^{-6}) and ice (50×10^{-6}) will counteract the expanded volume by (50-10) $\times10^{-6}\times20\times3\times0.12$=288μ, which is around 10% of total expanded volume. For the AE-concrete, for example, 6% AE, the hydraulic pressure can be totally released, and the cryosuction pressure is the main driving force. If we believe the cryosuction pressure can be up to -10 to -20 MPa, the effect of different thermal expansion coefficients is still negligible.

Appendix B. Strong contraction in pore water when ice forms

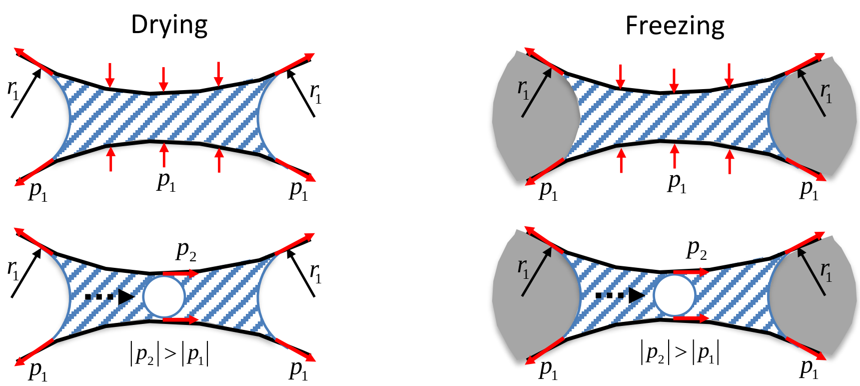

Fig. 17 Strong contraction in pore water during drying and freezing

During the drying process, water in bigger pores evaporates first. Based on the Kelvin equation and Laplace's law, RH=0.8 corresponds to a capillary pressure of -30Mpa and critical radius of 5nm. If adopting -0.5Mpa as the maximum tensile strength of pore water, only the pores bigger than 300nm can be dried with a retracting meniscus. Hence the drying from smaller pores must be from surface adsorbed state (or some other state different from liquid water) which is not likely since 300 nm corresponds to some 1000 layers of water molecules assuming molecular size in the order of 0.3 nm. In Fig. 17 we show both water-air interface and water-ice interface. Water-ice is in Fig.4 shown both with ice crystal forming in the full capillary ("submerged" in capillary water) and at the interface between empty air void and full capillary pore. If we add a smaller pore with meniscus close / next to the air water-interface (or if cavitation happens in a smaller space as indicated in Fig.17) compared to the critical radius (r_1), the pore water suction due to surface tension of air-water at the smaller pore or cavitation interface (p_2) is stronger than p_1, which cannot be stable. Unless the cavitation happens rapidly and everywhere (but this contradicts with the common adsorption/desorption isotherm), the pressure gradient caused by p_1 and p_2 will drive the flow and finally the pressures are balanced and the cavitated bubble may disappear.

The surface tension of liquid water during freezing behaves similarly as in the drying process, see lower part of Fig. 4 and right part of Fig. 17. The smaller the pore with an ice crystal forming from the air void the lower the temperature needed to form ice and the stronger the suction between the ice crystal and the capillary-/meso pore water, see also Sun and Scherer [15] etc.

References

[1] V. Hartmann, Optimizing and calibration of frost salt scaling testing of concrete CDF-test., University GH Essen, 1993, pp. 128.

[2] S. Jacobsen, E. Sellevold, Frost/salt scaling testing of concrete-importance of absorption during test, Nordic Concrete Research, 14 (1994) 26-44.

[3] S. Jacobsen, Dr. Ing. thesis 101, Norwegian Inst. of Technology, 1995, pp. 286.

[4] S. Jacobsen, D.H. Sœther, E.J. Sellevold, Frost testing of high strength concrete: frost/salt scaling at different cooling rates, Materials and structures, 30 (1997) 33-42.

[5] D.H. Bager, Freeze-thaw damage and water-uptake in low water/cement ratio concrete., Structural Engineering and Materials–A Centenary Celebration, (2000) 119-130.

[6] R. Auberg, and Setzer, M., Influence of water uptake during freezing and thawing., Frost Resistance of Concrete, 34 (2004) 251.

[7] T. Sandström, Fridh, K., Emborg, M., and Hassanzadeh, M. , The influence of temperature on water absorption in concrete during freezing., Nordic Concrete. Research, 45 (2012).

[8] Z. Liu, W. Hansen, Freezing characteristics of air-entrained concrete in the presence of deicing salt, Cement and Concrete Research, 74 (2015) 10-18.

[9] Z. Liu, W. Hansen, Effect of hydrophobic surface treatment on freeze-thaw durability of concrete, Cement and Concrete Composites, 69 (2016) 49-60.

[10] S. Jacobsen, F. Melandsø, H.T. Nguyen, Flow calculation and thermodynamics in wet frost exposure of cement based materials, Proc., International RILEM Symposium on Concrete Science and Engineering: A Tribute to Arnon Bentur, 2004.

[11] G.W. Scherer, J.J. Valenza II, Mechanisms of frost damage, Materials Science of Concrete, American Ceramic Society2005, pp. 209-246.

[12] Z. Yang, W.J. Weiss, J. Olek, Water transport in concrete damaged by tensile loading and freeze–thaw cycling, Journal of materials in civil engineering, 18 (2006) 424-434.

[13] O. Coussy, Poromechanics of freezing materials, Journal of the Mechanics and Physics of Solids, 53 (2005) 1689-1718.

[14] M. Matsumoto, S. Hokoi, M. Hatano, Model for simulation of freezing and thawing processes in building materials, Building and Environment, 36 (2001) 733-742.

[15] Z. Sun, G.W. Scherer, Effect of air voids on salt scaling and internal freezing, Cement and Concrete Research, 40 (2010) 260-270.

[16] Z. Sun, G.W. Scherer, Pore size and shape in mortar by thermoporometry, Cement and Concrete Research, 40 (2010) 740-751.

[17] F. Gong, K. Maekawa, Multi-scale simulation of freeze-thaw damage to RC column and its restoring force

characteristics, Engineering Structures, 156 (2018) 522-536.
[18] S. Jacobsen, E.J. Sellevold, S. Matala, Frost durability of high strength concrete: effect of internal cracking on ice formation, Cement and Concrete Research, 26 (1996) 919-931.
[19] O. Coussy, Mechanics and physics of porous solids, John Wiley & Sons2011.
[20] M.T. Van Genuchten, A closed-form equation for predicting the hydraulic conductivity of unsaturated soils, Soil science society of America journal, 44 (1980) 892-898.
[21] Q. Zeng, K. Li, T. Fen-Chong, Effect of supercooling on the instantaneous freezing dilation of cement-based porous materials, Journal of Building Physics, (2016) 1744259116649321.
[22] S. Poyet, Describing the influence of temperature on water retention using van Genuchten equation, Cement and Concrete Research, 84 (2016) 41-47.
[23] A. Hanaor, Testing of concrete specimens for permeability at cryogenic temperatures, Magazine of Concrete Research, 34 (1982) 155-162.
[24] T.C. Powers, A working hypothesis for further studies of frost resistance of concrete, ACI Journal Proceedings, ACI, 1945, pp. 245-272.
[25] O. Coussy, P.J.M. Monteiro, Errata to "Poroelastic model for concrete exposed to freezing temperatures" [Cement and Concrete Research 38 (2008) 40–48], Cement and Concrete Research, 39 (2009) 371-372.
[26] G. Fagerlund, On the service life of concrete exposed to frost action, Report TVBM (Intern 7000-rapport), (1993).
[27] K. Takewaka, T. Yamaguchi, S. Maeda, Simulation model for deterioration of concrete structures due to chloride attack, Journal of Advanced Concrete Technology, 1 (2003) 139-146.
[28] F. Gong, D. Zhang, E. Sicat, T. Ueda, Empirical estimation of pore size distribution in cement, mortar, and concrete, Journal of Materials in Civil Engineering, 26 (2013) 04014023.
[29] M.A.B. Promentilla, T. Sugiyama, X-ray microtomography of mortars exposed to freezing-thawing action, Journal of Advanced Concrete Technology, 8 (2010) 97-111.
[30] P. Fonseca, G. Scherer, An image analysis procedure to quantify the air void system of mortar and concrete, Materials and Structures, 48 (2015) 3087-3098.
[31] L.A. Crum, Tensile strength of water, Nature, 278 (1979) 148-149.
[32] N.P. Mayercsik, M. Vandamme, K.E. Kurtis, Assessing the efficiency of entrained air voids for freeze-thaw durability through modeling, Cement and Concrete Research, 88 (2016) 43-59.
[33] S. Rahman, Z. Grasley, Determining optimum air-void spacing requirement for a given concrete mixture design using poromechanics, International Journal of Pavement Engineering, (2016) 1-10.
[34] W. Vichit - Vadakan, G.W. Scherer, Measuring Permeability of Rigid Materials by a Beam - Bending Method: III, Cement Paste, Journal of the American Ceramic Society, 85 (2002) 1537-1544.
[35] G.W. Scherer, J.J. Valenza, G. Simmons, New methods to measure liquid permeability in porous materials, Cement and concrete research, 37 (2007) 386-397.
[36] F. Gong, E. Sicat, T. Ueda, D. Zhang, Meso-scale Mechanical Model for Mortar Deformation under Freeze Thaw Cycles, Journal of Advanced Concrete Technology, 11 (2013) 49-60.
[37] F. Gong, E. Sicat, D. Zhang, T. Ueda, Stress analysis for concrete materials under multiple freeze-thaw cycles, Journal of Advanced Concrete Technology, 13 (2015) 124-134.
[38] M.J. Setzer, A. Liebrecht, Modeling and Testing the Freeze-Thaw Attack by Micro-Ice-Lens Model and CDF/CIF Test, Proceedings of the International Workshop on Microstructure and Durability to Predict Service Life of Concrete Structures, 2004, pp. 17-28.
[39] S. Jacobsen, H.C. Gran, E.J. Sellevold, J.A. Bakke, High strength concrete—freeze/thaw testing and cracking, Cement and concrete research, 25 (1995) 1775-1780.
[40] M. Hasan, H. Okuyama, Y. Sato, T. Ueda, Stress-strain model of concrete damaged by freezing and thawing cycles,

Journal of Advanced Concrete Technology, 2 (2004) 89-99.
[41] S. Jacobsen, E. Sellevold, Frost testing high strength concrete: Scaling and cracking, Fourth International Symposium on the Utilization of High Strength/High Performance Concrete, 1996, pp. 597-605.